scientific reports

Check for updates

OPEN

Topological electromagnetic waves in dispersive and lossy plasma crystals

Chen Qian[1,4], Yue Jiang[1,4], Jicheng Jin[1], Thomas Christensen[2], Marin Soljačić[2], Alexander V. Kildishev[3] & Bo Zhen[1]✉

Topological photonic crystals, which offer topologically protected and back-scattering-immune transport channels, have recently gained significant attention for both scientific and practical reasons. Although most current studies focus on dielectric materials with weak dispersions, this study focuses on topological phases in dispersive materials and presents a numerical study of Chern insulators in gaseous-phase plasma cylinder cells. We develop a numerical framework to address the complex material dispersion arising from the plasma medium and external magnetic fields and identify Chern insulator phases that are experimentally achievable. Using this numerical tool, we also explain the flat bands commonly observed in periodic plasmonic structures, via local resonances, and how edge states change as the edge termination is periodically modified. This work opens up opportunities for exploring band topology in new materials with non-trivial dispersions and has potential radio frequency (RF) applications, ranging from plasma-based lighting to plasma propulsion engines.

The discovery that topological phases can exist beyond electronics[1–3] has garnered significant attention in other wave systems such as photonics[4–6], plasmonics[7–9], polaritonics[10], acoustics[11,12], and even water waves[13,14]. Of particular interest is the quantum anomalous Hall effect, also known as Chern insulators, which can offer topologically protected transport channels and immunity against back-scattering at the interface with normal insulators. Such transport channels have both scientific inquiry and practical applications in fields such as optical communication, low-loss waveguides, and circulators.

To create photonic Chern insulators, time-reversal symmetry must be broken while retaining near-Hermiticity. This requires a permittivity or permeability tensor that breaks reciprocity, such that $\boldsymbol{\varepsilon}^{\mathrm{T}} \neq \boldsymbol{\varepsilon}$ or $\boldsymbol{\mu}^{\mathrm{T}} \neq \boldsymbol{\mu}$. The properties of the underlying materials, along with their geometric aspects, determine the topological invariants (Chern numbers) of the electromagnetic band gaps and their transport properties.

Most current studies of photonic Chern insulators have relied on gyromagnetic materials (e.g. yttrium iron garnet[2,15–17]) and external magnetic fields. These materials are mostly dielectric in nature, meaning their permeability remains positive in the frequency range of interest, resulting in Bloch modes that are delocalized in the photonic crystals. There has been recent interest in gyroelectric materials, which have the potential for large Faraday effects in magnetized plasmas in metals. This focus has centered on continua[18] and plasmonic crystals[7–9], where the Chern insulator phase is mostly composed of coupled plasmonic resonances localized at individual sites with Drude-like material responses and negative permittivity.

Here, we present a numerical study of photonic Chern insulators in plasma crystals with gaseous-phase plasma, which simultaneously exhibit both extended photonic bands and localized plasmonic modes in the RF regime. Our design is based on a 2D crystal of plasma cells placed in an external magnetic field. Without the magnetic field, the responses of the plasma elements are Drude-like, and the associated structure is known to support coexisting de-localized and localized modes in suitable polarizations[19–21]. We explore the time-reversal broken generalization, which exhibits an interesting interplay between the Drude and Lorentzian dispersion due to the applied magnetic field causing cyclotron motions in the plasma. We propose a plasma crystal design that features a Chern insulator gap between de-localized photonic bands, coexisting with nearby dense groups of flat bands associated with localized plasmons of fixed-handedness. On termination of this crystal, we observe a rich interplay between localized plasmonic bands and de-localized chiral edge states inside the Chern insulating gap.

[1]Department of Physics and Astronomy, University of Pennsylvania, Philadelphia 19104, USA. [2]Massachusetts Institute of Technology, Department of Physics, Cambridge 02139, USA. [3]Elmore Family School of Electrical and Computer Engineering, Purdue University West Lafayette, Birck Nanotechnology Center and Purdue Quantum Science and Engineering Institute (PQSEI), West Lafayette 47907, USA. [4]These authors contributed equally: Chen Qian and Yue Jiang. ✉email: bozhen@sas.upenn.edu

Finally, we explore how local and de-localized edge modes evolve under continuous deformations of the interface between the Chern insulator and perfect magnetic conductors. The mode evolution can then be interpreted as a manifestation of the filling anomalies.

Our work is organized as follows: first, we review the plasma dispersion without and with an external magnetic field. Then, we present the band structure of plasma crystals without and with an external magnetic field and their associated topological invariants. Next, we explain the origin of the observed flat bands in calculations as localized surface plasmon polariton resonances. Afterward, we explore how the chiral edge state dispersion evolves when the edge termination changes. Finally, we discuss the limitations existing in our calculations and practical aspects related to the experimental verification of our proposal.

Results

Dispersion of plasma without magnetic field: drude model

We start by presenting a comprehensive review of the dispersion properties of the plasma permittivity (ε) by employing the widely accepted Drude model[22]. In our analysis, we made the fundamental assumption that the positive ions within the plasma are significantly heavier and thus remain immobile. Consequently, the contribution to the volume current density (J) is exclusively attributed to the movement of electrons: $\mathbf{J} = -ne\mathbf{v}$. In this equation, n represents the volume density of electrons, and $-e$ corresponds to the electron charge of an individual electron. The equation of motion for electrons in the plasma crystals reads:

$$m_e \partial_t \mathbf{J} + \gamma m_e \mathbf{J} = ne^2 \mathbf{E}. \tag{1}$$

Here, m_e is the electron mass, γ is the damping rate, and $\mathbf{E}$ is the electric field. For harmonic solutions at a fixed angular frequency ω, all temporal derivatives can be substituted via $\partial_t \rightarrow -i\omega$. Accordingly, the frequency-dependent plasma conductivity σ can be written as

$$\mathbf{J} = \left(\frac{\varepsilon_0 \omega_p^2}{-i\omega + \gamma} \right) \mathbf{E} = \sigma \mathbf{E}. \tag{2}$$

Here, $\omega_p = \sqrt{\frac{ne^2}{m_e \varepsilon_0}}$ is the plasma frequency. Noting that the volume current density is also related to the electric polarization: $\mathbf{J} = \partial_t \mathbf{P} = -i\omega \mathbf{P}$, the Drude permittivity of plasma ε can be defined as:

$$\mathbf{D} = \varepsilon_0 \mathbf{E} + \mathbf{P} = \left(\varepsilon_0 + \frac{i\sigma}{\omega} \right) \mathbf{E} = \varepsilon_0 \left[1 - \frac{\omega_p^2}{\omega(\omega + i\gamma)} \right] \mathbf{E}. \tag{3}$$

Dispersion of magnetized plasma

Following these steps, we calculated the permittivity tensor describing gaseous phase plasma placed in an external magnetic field (Fig. 1a). Following Eq. (3), we need to re-write the conductivity tensor ($\bar{\bar{\sigma}}$), based on the updated equation of motion for electrons. Considering the Lorentz force, the equation of motion becomes:

$$m_e \partial_t \mathbf{J} + m_e \gamma \mathbf{J} = ne^2 \mathbf{E} + e\mathbf{J} \times B\hat{\mathbf{z}} \tag{4}$$

Re-writing the equation in circular bases in the xy plane: $(J_+, J_-, J_z) = (\frac{J_x + iJ_y}{\sqrt{2}}, \frac{J_x - iJ_y}{\sqrt{2}}, J_z)$ and $(E_+, E_-, E_z) = (\frac{E_x + iE_y}{\sqrt{2}}, \frac{E_x - iE_y}{\sqrt{2}}, E_z)$, both matrices $\bar{\bar{\sigma}}$ and $\bar{\bar{\varepsilon}}$ become diagonal. Specifically, the conductivity tensor $\bar{\bar{\sigma}}$ can be expressed as:

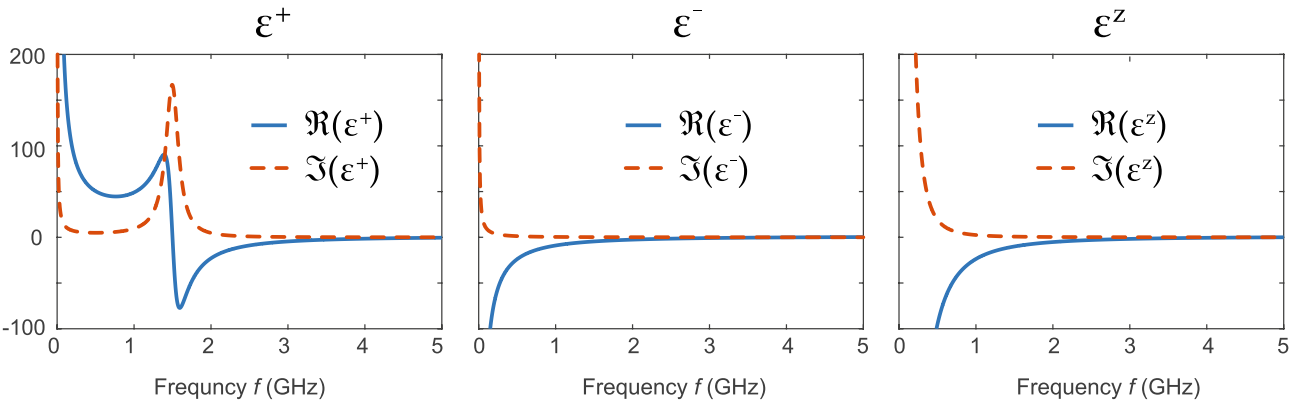

Figure 1. Permittivity dispersion of plasma medium in an external magnetic field. ε_+ (ε_-) is the permittivity of right-handed (left-) circular polarization under an external magnetic field of 0.054 T. ε_z is for polarization along the z direction. The real and imaginary parts of the permittivity are shown in blue and red, respectively. Both ε_+ and ε_- are affected by the cyclotron resonance at $f_c = 1.5$ GHz, while ε_z is unaffected and remains to be given by the standard Drude model.

$$\begin{pmatrix} J_+ \\ J_- \\ J_z \end{pmatrix} = \mathrm{i}\varepsilon_0\omega_\mathrm{p}^2 \begin{pmatrix} \frac{1}{\omega+\mathrm{i}\gamma-\omega_\mathrm{c}} & & \\ & \frac{1}{\omega+\mathrm{i}\gamma+\omega_\mathrm{c}} & \\ & & \frac{1}{\omega+\mathrm{i}\gamma} \end{pmatrix} \begin{pmatrix} E_+ \\ E_- \\ E_z \end{pmatrix}. \tag{5}$$

Here $\omega_\mathrm{c} = \frac{eB}{m_e}$ is the cyclotron resonance. Accordingly, the permittivity tensor of the magnetized plasma $\bar{\bar{\varepsilon}}$ has the following form in a Cartesian basis:

$$\bar{\bar{\varepsilon}} = \mathbf{U}^\dagger \begin{pmatrix} \varepsilon_+ & & \\ & \varepsilon_- & \\ & & \varepsilon_z \end{pmatrix} \mathbf{U}, \tag{6}$$

where the column vectors of the matrix U label the directions of the optical principle axes:

$$\mathbf{U} = \begin{pmatrix} \frac{1}{\sqrt{2}} & \frac{\mathrm{i}}{\sqrt{2}} & \\ \frac{\mathrm{i}}{\sqrt{2}} & \frac{1}{\sqrt{2}} & \\ & & 1 \end{pmatrix}. \tag{7}$$

Meanwhile, along the principal axes, the material dispersion can be expressed as:

$$\begin{aligned} \varepsilon_\pm &= \varepsilon_0 + \mathrm{i}\frac{\sigma_\pm}{\omega} = \varepsilon_0\left[1 - \frac{\omega_\mathrm{p}^2}{\omega(\omega+\mathrm{i}\gamma \mp \omega_\mathrm{c})}\right], \\ \varepsilon_z &= \varepsilon_0 + \mathrm{i}\frac{\sigma_\mathrm{z}}{\omega} = \varepsilon_0\left[1 - \frac{\omega_\mathrm{p}^2}{\omega(\omega+\mathrm{i}\gamma)}\right]. \end{aligned} \tag{8}$$

This outcome can be intuitively understood as follows: when subjected to an external magnetic field along the $\hat{\mathbf{z}}$ direction, electrons undergo cyclotron motion, forming orbits at a constant angular frequency of ω_c within the xy plane. In a co-rotating (counter-rotating) reference frame synchronized with the electrons, the induced electric field preserves the same (opposite) circular polarization but is slightly shifted in frequency by ω_c ($-\omega_\mathrm{c}$), yielding the distinctive properties ε_+ and ε_-, respectively. On the other hand, the electric field applied in the z direction remains unaffected by the cyclotron motion. Consequently, the dispersion of ε_z maintains the conventional characteristics of the standard Drude dispersion.

Next, we numerically compute the material dispersion as functions of frequency $f = \omega/2\pi$ using the typical values in gaseous phase plasma. The results are shown in Fig. 1, where the external magnetic field is set at 0.054 T and the corresponding cyclotron resonance is at $f_\mathrm{c} = \omega_\mathrm{c}/2\pi = 1.5\,\mathrm{GHz}$. The plasma frequency is controlled by the number density of electrons, which is set to be a practical value of $n = 3.1 \times 10^{11}\,\mathrm{cm}^{-3}$ throughout the calculations. Accordingly, the plasma frequency is at $f_\mathrm{p} = \omega_\mathrm{p}/2\pi = 5\,\mathrm{GHz}$. The real and imaginary parts of the permittivity are shown in blue and red, respectively. The parameter γ refers to the damping rate, which mostly originates from the electron-ion collisions at room temperature. For helium plasma gas, the damping rate is roughly linearly proportional to the gas pressure: $\gamma = 0.318\,\mathrm{GHz\,Torr}^{-1} \times p$. Using a practical pressure of $p = 0.314$ Torr, the damping is set to be $\gamma = 0.1$ GHz throughout our calculations.

As expected from Eq. (8), both ε_+ and ε_- are affected by the cyclotron resonance and deviate from the standard Drude model (ε_z). For example, at low frequencies ($f \approx 0$), ε_+ is positive and diverges as $1/f$; ε_- is negative and diverges as $1/f$; meanwhile, the Drude model ε_z is negative and diverges as $1/f^2$. These fundamental differences in scaling lead to challenges when fitting the dispersion to standard formalism in commercial software, as described later.

We note that our description of the plasma medium is limited by a few approximations. Overcoming these approximations would lead to modifications of our results and will be discussed elsewhere. First, only electrons are assumed to move under the influence of external electromagnetic fields, while ions are assumed to be always stationary. Second, our permittivity ignores non-local effects, which leads to a frequency gap between surface plasmon polaritons traveling in opposite directions[23–25]. Finally, we neglect the inhomogeneous broadening effect, and thus the bandwidth of our permittivity is defined solely by electron damping.

Band structures of plasma crystals without external magnetic field

Utilizing the dispersion equation outlined in Eq. (8)[26], we compute the band structure associated with a square lattice comprising plasma cylinders positioned within an air medium. Our investigation primarily centered around quadratic point degeneracy, a distinctive phenomenon safeguarded by both spatial symmetry and time-reversal symmetry. This quadratic point is important in our study, as it arises from the combined effects of spatial symmetry (C_4) and time-reversal symmetry (T), which is broken when T is broken.

The plasma photonic crystal unit cell is shown in Fig. 2a, where the lattice constant a is 6 cm, and the radius of the cylinder r is 1.5 cm. The external magnetic field along the z direction preserves the mirror symmetry in z (σ_z) and separates the electromagnetic modes into two mode types: to avoid possible terminology confusion, we follow the definition of Sakoda[27] to distinguish the E-polarization case (with the **E**-field parallel to the z-axis) from the H-polarization case (with the **H**-field parallel to the z-axis). We also use the E-case and H-case for short. Given that the gyroelectric response has response components only in the xy-plane but not along the z-direction [Eq. (5)], we focus solely on the H-case and disregard the associated E-case.

Without breaking time-reversal symmetry (T), i.e., $B = 0$, the plasma dispersion follows the standard Drude model, and the H-case can be calculated using a standard finite element method (FEM). The results are plotted

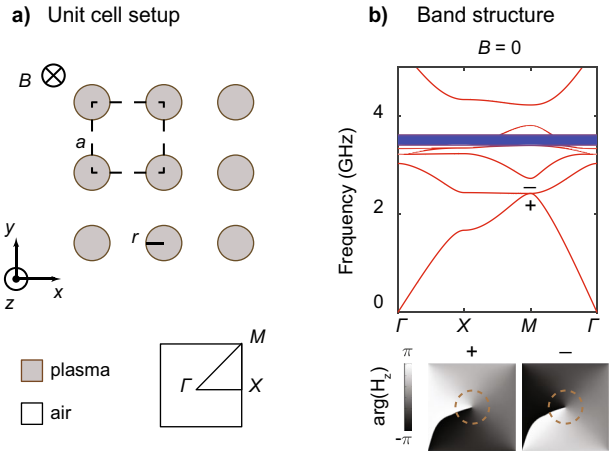

Figure 2. Real part of the band structure of a plasma photonic crystal without external magnetic field. (**a**) Schematic drawing of a photonic crystal made of gaseous plasma cylinders placed in the air. (**b**) Calculated H-case without magnetic field ($B = 0$), where a quadratic degeneracy, modes '+' and '−', with $C_{4z} = \pm i$ respectively, is found at the Brillouin zone corner. A set of flat bands (blue ribbon) are also observed in the calculation.

along high-symmetry lines in the Brillouin zone (Fig. 2b). As shown, a pair of quadratic degeneracies are found at the M point in the Brillouin zone around 2.4 GHz, which is protected by the 90-degree rotation symmetry C_{4z} and T. Specifically, the two modes, marked as '+' and '−', have C_{4z} indices of $\pm i$,. They are connected to each other by T. The phases of the corresponding mode profiles, arg(H_z), confirm the C_{4z} indices of the two modes. We note that a set of flat bands is observed in the calculation (blue ribbon) with an upper-frequency bound of $f_p/\sqrt{2} = 3.5$ GHz, which is further discussed in the next section.

Band structure of the magnetized-plasma photonic crystals and Chern insulators

In the presence of an external magnetic field, the behavior of the plasma dispersion (ε_+ and ε_-) deviates from the conventional Drude model. This alteration introduces complexities that pose challenges for accurately representing the band structure using standard material dispersion models available in commercial software solutions. As a result, we modify a standard Finite Element Method (FEM) technique to effectively capture the intricacies of the band structure, especially concerning band crossings that demand precise resolution. Following conventional methodologies (e.g., in[28–32]), we applied Floquet periodic boundary conditions in the 2D spatial domain. This technique allowed us to address a quadratic eigenvalue problem within a square unit cell configuration, as illustrated in Fig. 2a. To solve this problem, we discretized the unit cell to formulate a weak FEM approach. Our computational process leveraged COMSOL Multiphysics™, a versatile software platform adept at constructing customized systems of coupled equations. For the numerical eigenvalue computations, we integrated the Portable Large Scale Eigenvalue Package (P_ARPACK)[33]. P_ARPACK, which is a parallel implementation derived from the ARPACK software[34]. P_ARPACK employs the Implicitly Restarted Arnoldi Method (IRAM) and is particularly suited for tackling large sparse eigenvalue problems, even when constrained by specific eigenvalue counts. The combination of COMSOL Multiphysics™ and P_ARPACK facilitated the development of a scalable and efficient eigenvalue solver, making it feasible to tackle the customized quadratic eigenvalue problems arising from our research. The adaptability of the software, coupled with its user-friendly interface, allowed us to fine-tune key parameters of the IRAM-based solver according to our requirements. Furthermore, the efficiency of employing P_ARPACK within the COMSOL framework for addressing customized quadratic eigenvalue problems has been demonstrated by multiple studies, exemplified by references[31,35,36]. This substantiates the reliability and advantages of our chosen approach for solving complex eigenvalue problems in our research context.

In contrast to the known methods largely employing the auxiliary equations for the polarization vector, we couple *the weak-form equations for the current density and the* **E***-field*, achieving a stable performance with flexible tracking of a desired number of bands and unambiguous resolution of the band crossings. We have provided a general equation for current density under an external magnetic field. In the H-case, we directly use the External Current Density Interface with an auxiliary algebraic equation (AE) for in-plane vectors,

$$\mathbf{J}_{xy} = \left(J_x, J_y\right)^{\mathrm{T}},\ \mathbf{E}_{xy} = \left(E_x, E_y\right)^{\mathrm{T}} \tag{9}$$

We then employ a normalized current density $\mathbf{j}_{xy} = \mathbf{J}_{xy}/\left(\varepsilon_0\omega_p^2\right)$ in a normalized Drude model

$$\left(\omega_c^2 - (\omega + \mathrm{i}\gamma)^2\right)\mathbf{j}_{xy} - \mathrm{i}\begin{pmatrix} \omega + \mathrm{i}\gamma & -\mathrm{i}\omega_c \\ \mathrm{i}\omega_c & \omega + \mathrm{i}\gamma \end{pmatrix}\mathbf{E}_{\mathrm{xy}} = 0 \tag{10}$$

The weak form is obtained by integrating the dot product of Eq. (10) with an arbitrary test function $\mathbf{j}_{xy} = \text{test}(\mathbf{j}_{xy})$ over the Drude material domain,

$$\int_\Omega \left((\omega_c^2 - (\omega + i\gamma)^2)\mathbf{j}_{xy} - i \begin{pmatrix} \omega + i\gamma & -i\omega_c \\ i\omega_c & \omega + i\gamma \end{pmatrix} \mathbf{E}_{xy} \right) \cdot \mathbf{j}_{xy} \, d\Omega = 0 \tag{11}$$

An auxiliary equation for the current density is introduced to the COMSOL framework through the Weak Contribution interface,

$$F = i\omega k_p^2 (\mathbf{j}_{xy} \cdot \mathbf{E}_{xy}) \tag{12}$$

where $\mathbf{E}_{xy} = \text{test}(\mathbf{E}_{xy})$ is the $\mathbf{E}$-field test function and $k_p = \omega_p/c$ is the plasma wave number. The approach exhibits good error convergence with accuracy controlled through the meshing density and the FE order. In contrast with[31,35–38] we completely exclude the polarization vector, reducing the order of the auxiliary equations and improving the numerical accuracy at $\omega \to 0$. The full details on the numerical implementation and verification of the IRAM-based eigensolver are not the main focus of the paper and these details will be published elsewhere.

An example of the calculated band structures is shown in Fig. 3a when the external magnetic field is set to be $B = 0.054$ T. As time-reversal symmetry T is broken, the M-point degeneracy is lifted, opening an 8% full energy gap, from 2.18 to 2.37 GHz (green ribbon). As the structure still maintains C_{4z} symmetry, the Chern number C of the first band is necessarily non-trivial[39], since

$$e^{i\pi C} = C_{2z}(\Gamma) \times C_{2z}(M) = -1, \tag{13}$$

where C_{2z} is the phase change of the mode profile after a π-rotation. $C_{2z}(\Gamma) = 1$ since the phase of an electromagnetic wave is locked at zero frequency, and $C_{2z}(M) = -1$ because it originates from the time-reversal symmetry breaking of the degenerate modes shown in Fig. 2b. As a result, the first gap highlighted in green corresponds to a Chern insulator[40] and supports unidirectional transport channels, as shown next. Due to the magnetic field, the flat bands split into two regions (two blue ribbons), as explained in detail in the next section.

Flat bands from localized surface plasmon polariton resonances

In this section, we elucidate the origin of the flat bands observed above, from the viewpoint of localized surface plasmon polaritonic (SPP) resonances. We note that such flat band features are also commonly observed elsewhere, such as in metallic photonic crystals[28]. The one unusual feature is related to the splitting of flat band regions under an external magnetic field (Fig. 3a).

It is more straightforward to understand the flat bands if we consider the local SPP resonances supported by a single plasma cylinder[7,8]. As the cylinder has full rotation symmetry, the SPP resonances can be labeled by different azimuthal numbers, m, corresponding to different angular momenta. A few interesting features can be observed in Fig. 3b. First, the resonances with negative m (orange dots, rotating counter-clockwise) are at higher frequencies than the resonances with positive m (blue dots, clockwise). Second, the local SPP resonance frequency generally increases with $|m|$, approaching different bounds near the two ends: $(\sqrt{f_c^2 + 2f_p^2} + f_c)/2 = 4.4$ GHz when m approaches $-\infty$ and $(\sqrt{f_c^2 + 2f_p^2} - f_c)/2 = 2.9$ GHz when m approaches $+\infty$. Finally, the resonances with larger $|m|$s are better localized in space than the resonances with smaller $|m|$. Such a trend can be well observed in the comparison between the mode profile of $m = -5$ (more localized) versus the model profile of $m = 1$ (more extended, inset of Fig. 3b). Taken together, at large $|m|$, the SPP resonances are tightly confined to

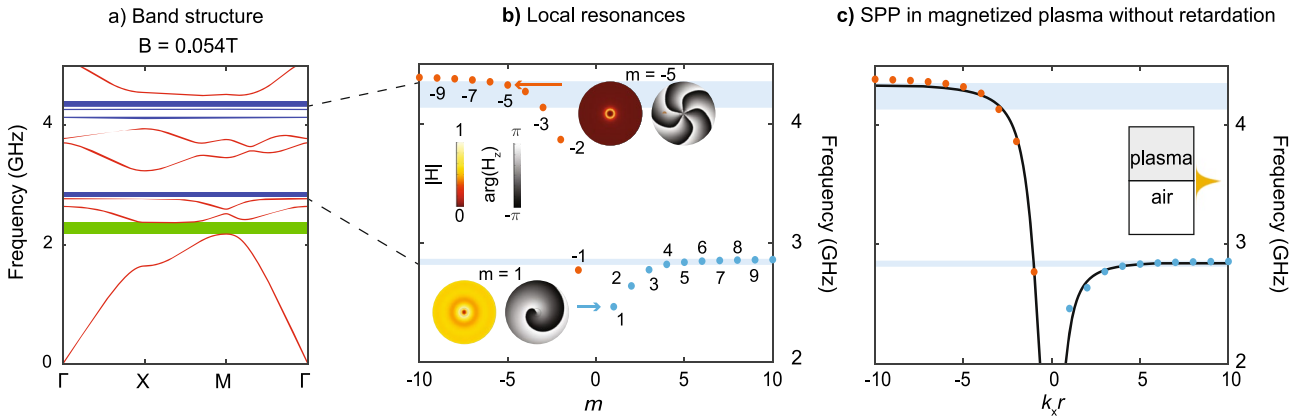

Figure 3. Real part of the band structure of magnetized-plasma photonic crystal featuring a Chern insulator gap. (**a**) Under an external magnetic field of $B = 0.054$ T, a full energy gap is opened (green ribbon), featuring a non-zero Chern number. Meanwhile, the flat bands split into two groups (blue ribbons). (**b**) Local resonances, labeled by different azimuthal numbers m, are responsible for observed flat bands in (**a**). Two example mode profiles ($m = 1$ and $m = -5$) are shown, both in amplitude (hot color map) and phase (gray-scale). (**c**) The frequency of local resonances agrees well with the surface plasmon polariton (SPP) dispersion at the interface between air and magnetized plasma.

individual cylinders, resulting in minimal modal overlaps. This limited overlap leads to reduced dispersion, which, in turn, results in the formation of flat bands. Thus, each flat band corresponds to a different m. Furthermore, the frequency of the flat bands (blue ribbons) also splits into two regions, approaching the two frequency bounds mentioned above.

Here we note that the number of calculated flat bands using our numerical method increases with increased mesh density—a common feature also observed in the literature[28]—although the frequency of the flat bands is always confined to the blue regions. Furthermore, the reliable azimuthal number of calculated modes is always limited by the numerical resolution. In our specific setting, modes with $|m| > 10$ are no longer reliable. See Supplementary Information for more details.

Finally, we verify the local SPP resonance frequencies in each plasma cylinder using the SPP dispersion along the interface between air and magnetized plasma, where a good agreement is found (Fig. 3c). The momentum of each local SPP resonance is determined as m/r, where m is the azimuthal number and r is the radius of the cylinder.

Evolution of the chiral edge state dispersion with changing edge termination

While the existence of chiral edge states (CES) is guaranteed at the interface between a Chern insulator and a trivial insulator, their exact dispersion depends on the details of the interface. In this section, we continuously change the interface configuration and study how the CES dispersion evolves accordingly. Our finding suggests that CES dispersion essentially reflects that a localized plasma resonance emerges at the interface when the plasma is cut through, and the frequency of the antenna state decreases with the shrinking of the plasma region.

The dispersion of Chiral Edge States (CES) is computed through interactions at the interfaces between a Chern insulator super-cell and a pair of perfect magnetic conductors (PMC), as visualized in Fig. 4. Each unit cell within the Chern insulator preserves the identical design and parameters presented in Fig. 3. The arrangement entails a fixed lower interface (blue), while the upper interface (red) is systematically adjusted by incrementing the distance d from 0 to a. Beginning with $d/a = 0$, a significant outcome is observed in the super-cell dispersion-two CES bands materialize. One is located at the upper interface (red), and the other emerges at the lower interface (blue). As the ratio d/a increases, the CES located at the upper interface (red) progresses in frequency, ascending until the PMC interacts with the plasma cell at $d/a = 0.25$. With further increments in d/a, the high-frequency section of the CES remains relatively unchanged while the low-frequency component continues ascending. This trend persists until $d/a = 0.5$ where the PMC bisects the plasma cell. As d/a continues to rise, the CES dispersion transforms into a progressively flatter profile.

At d/a=0.7, the CES dispersion undergoes a pivotal change-dividing into two bands. One of these bands traverses the topological gap and retains CES characteristics, while the other is a trivial band existing outside the

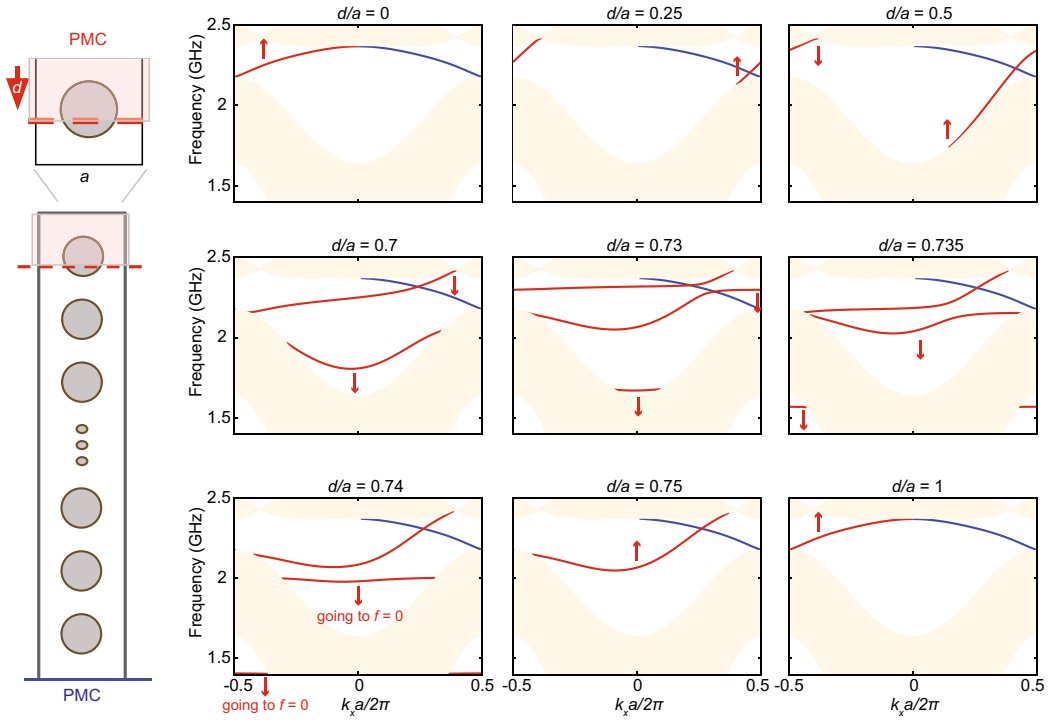

Figure 4. Evolution of chiral edge states as the interface changes. A super-cell of electromagnetic Chern insulator (same design as in Fig. 3) is terminated by PMC. The bottom interface (blue) is fixed, while the top interface (red) changes from $d/a = 0$ to $d/a = 1$. The corresponding chiral edge states (CES) dispersion under different configurations of d/a is shown on the right. Red arrows indicate the evolution direction of the CES.

topological gap. A second splitting transpires at $d/a = 0.735$, yielding an additional trivial band. As the distance d/a increases further, both trivial bands descend in frequency, crossing through the initial bulk continuum and eventually vanishing at zero frequency $f = 0$ when $d/a = 0.75$. See Supplementary Information for the case when $d/a = 0.74996$. Upon reaching d/a=1, the interface configuration regresses to the $d/a = 0$ arrangement, leading the CES dispersion to revert to its initial configuration.

In essence, this detailed description captures the intricate evolution of CES dispersions as the distance d is varied in relation to the unit cell size a. The interplay between interface configurations and distance ratios results in a rich spectrum of phenomena and transitions.

Discussion

Our simulation has a few limitations that should be noted. Firstly, the ions are assumed to be stationary and not moving, i.e., only electrons are allowed to move under the external fields. Introducing ions' motion would lead to an effective mass and lower plasma frequency. Secondly, our permittivity model ignores non-local effects, which results in a frequency gap between surface plasmon polaritons traveling in opposite directions[23,24]. Thirdly, we have neglected the inhomogeneous broadening effect in the plasma, and the bandwidth of our permittivity is contributed solely by electron damping. Introducing the inhomogeneous broadening effect would further broaden the energy bands and reduce the effective size of the band gaps. It is also worth noting that the cyclotron frequency of the plasma at 1.5 GHz is much larger than the electron damping rate at 0.1 GHz, and hence the homogeneous broadening effect contributes solely to the broadening of the energy bands without qualitatively changing the band topology.

Despite these limitations, we believe that our proposal is feasible to demonstrate in an experiment. The required magnetic field of 0.314 T can be achieved, even over large areas, via commercial electromagnets or permanent magnets. Meanwhile, the required carrier number density of 3.1×10^{11} cm^{-3} and the pressure of 0.314 Torr are also within the typical range in experiments.

Data availability

The datasets generated during and/or analyzed during the current study are available from the corresponding author on reasonable request.

Received: 24 July 2023; Accepted: 19 November 2023
Published online: 22 November 2023

References

1. Haldane, F. D. M. & Raghu, S. Possible realization of directional optical waveguides in photonic crystals with broken time-reversal symmetry. *Phys. Rev. Lett.* **100**, 013904. https://doi.org/10.1103/PhysRevLett.100.013904 (2008).
2. Wang, Z., Chong, Y., Joannopoulos, J. D. & Soljačić, M. Observation of unidirectional backscattering-immune topological electromagnetic states. *Nature* **461**, 772–775. https://doi.org/10.1038/nature08293 (2009).
3. Lu, L., Joannopoulos, J. D. & Soljačić, M. Topological photonics. *Nat. Photonics* **8**, 821–829. https://doi.org/10.1038/nphoton.2014.248 (2014).
4. Sigalas, M. M., Chan, C. T., Ho, K. M. & Soukoulis, C. M. Metallic photonic band-gap materials. *Phys. Rev. B* **52**, 11744–11751. https://doi.org/10.1103/PhysRevB.52.11744 (1995).
5. He, L., Addison, Z., Mele, E. J. & Zhen, B. Quadrupole topological photonic crystals.. *Nat. Commun.* **11**, 3119. https://doi.org/10.1038/s41467-020-16916-z (2020).
6. Lu, J., He, L., Addison, Z., Mele, E. J. & Zhen, B. Floquet topological phases in one-dimensional nonlinear photonic crystals. *Phys. Rev. Lett.* **126**, 113901. https://doi.org/10.1103/PhysRevLett.126.113901 (2021).
7. Jin, D. *et al.* Topological magnetoplasmon.. *Nat. Commun.* **7**, 13486. https://doi.org/10.1038/ncomms13486 (2016).
8. Jin, D. *et al.* Infrared topological plasmons in graphene. *Phys. Rev. Lett.* **118**, 245301. https://doi.org/10.1103/PhysRevLett.118.245301 (2017).
9. Pan, D., Yu, R., Xu, H. & de Abajo, F. J. G. Topologically protected Dirac plasmons in a graphene superlattice. *Nat. Commun.* **8**, 1243. https://doi.org/10.1038/s41467-017-01205-z (2017).
10. He, L., Wu, J., Jin, J., Mele, E. J. & Zhen, B. Polaritonic Chern insulators in monolayer semiconductors. *Phys. Rev. Lett.* **130**, 043801. https://doi.org/10.1103/PhysRevLett.130.043801 (2023).
11. Yang, Z. *et al.* Topological acoustics. *Phys. Rev. Lett.* **114**, 114301. https://doi.org/10.1103/PhysRevLett.114.114301 (2015).
12. Xue, H., Yang, Y. & Zhang, B. Topological acoustics. *Nat. Rev. Mater.* **7**, 974–990. https://doi.org/10.1038/s41578-022-00465-6 (2022).
13. Delplace, P., Marston, J. B. & Venaille, A. Topological origin of equatorial waves. *Science* **358**, 1075–1077. https://doi.org/10.1126/science.aan8819 (2017).
14. Perrot, M., Delplace, P. & Venaille, A. Topological transition in stratified fluids. *Nat. Phys.* **15**, 781–784. https://doi.org/10.1038/s41567-019-0561-1 (2019).
15. Wang, Z., Chong, Y. D., Joannopoulos, J. D. & Soljačić, M. Reflection-free one-way edge modes in a gyromagnetic photonic crystal. *Phys. Rev. Lett.* **100**, 013905. https://doi.org/10.1103/PhysRevLett.100.013905 (2008).
16. Skirlo, S. A., Lu, L. & Soljačić, M. Multimode one-way waveguides of large Chern numbers. *Phys. Rev. Lett.* **113**, 113904. https://doi.org/10.1103/PhysRevLett.113.113904 (2014).
17. Liu, G.-G. *et al.* Topological Chern vectors in three-dimensional photonic crystals. *Nature* **609**, 925–930. https://doi.org/10.1038/s41586-022-05077-2 (2022).
18. Silveirinha, M. G. Bulk-edge correspondence for topological photonic continua. *Phys. Rev. B* **94**, 205105. https://doi.org/10.1103/PhysRevB.94.205105 (2016).
19. Sakoda, K. *et al.* Photonic bands of metallic systems. I. Principle of calculation and accuracy. *Phys. Rev. B* **64**, 045116. https://doi.org/10.1103/PhysRevB.64.045116 (2001).
20. Ito, T. & Sakoda, K. Photonic bands of metallic systems. II. Features of surface plasmon polaritons. *Phys. Rev. B* **64**, 045117. https://doi.org/10.1103/PhysRevB.64.045117 (2001).
21. Raman, A. & Fan, S. Perturbation theory for plasmonic modulation and sensing. *Phys. Rev. B* **83**, 205131. https://doi.org/10.1103/PhysRevB.83.205131 (2011).
22. Swanson, D. G. *Plasma Waves, chap. 2* 2nd edn. (CRC Press, Boca Raton, 2003).

23. Kuzmiak, V. & Maradudin, A. A. Photonic band structures of one- and two-dimensional periodic systems with metallic components in the presence of dissipation. *Phys. Rev. B* **55**, 7427–7444. https://doi.org/10.1103/PhysRevB.55.7427 (1997).
24. Gangaraj, S. A. H. & Monticone, F. Do truly unidirectional surface plasmon-polaritons exist?. *Optica* **6**, 1158–1165. https://doi.org/10.1364/OPTICA.6.001158 (2019).
25. Buddhiraju, S. *et al.* Absence of unidirectionally propagating surface plasmon-polaritons at nonreciprocal metal-dielectric interfaces. *Nat. Commun.* **11**, 674. https://doi.org/10.1038/s41467-020-14504-9 (2020).
26. Howard, J. Introduction to Plasma Physics I—Collated Notes, 106 (Flooved.com, 2013), 1 edn. https://archive.org/details/flooved3263.
27. Sakoda, K. *Optical Properties of Photonic Crystals* 20th edn. (Springer, Berlin, 2005). https://doi.org/10.1007/b138376.
28. Kuzmiak, V., Maradudin, A. A. & Pincemin, F. Photonic band structures of two-dimensional systems containing metallic components. *Phys. Rev. B* **50**, 16835–16844. https://doi.org/10.1103/PhysRevB.50.16835 (1994).
29. Kuzmiak, V. & Maradudin, A. A. Distribution of electromagnetic field and group velocities in two-dimensional periodic systems with dissipative metallic components. *Phys. Rev. B* **58**, 7230–7251. https://doi.org/10.1103/PhysRevB.58.7230 (1998).
30. Degirmenci, E. & Landais, P. Finite element method analysis of band gap and transmission of two-dimensional metallic photonic crystals at terahertz frequencies. *Appl. Opt.* **52**, 7367–7375. https://doi.org/10.1364/AO.52.007367 (2013).
31. Yan, W., Faggiani, R. & Lalanne, P. Rigorous modal analysis of plasmonic nanoresonators. *Phys. Rev. B* **97**, 205422. https://doi.org/10.1103/PhysRevB.97.205422 (2018).
32. Xiao, W. & Sun, J. Band structure calculation of photonic crystals with frequency-dependent permittivities. *J. Opt. Soc. Am. A* **38**, 628–633. https://doi.org/10.1364/JOSAA.412235 (2021).
33. Maschhoff, K. J. & Sorensen, D. C. P_ARPACK: An efficient portable large scale eigenvalue package for distributed memory parallel architectures. In *Applied Parallel Computing Industrial Computation and Optimization* (eds Waśniewski, J. *et al.*) 478–486 (Springer, Berlin, 1996).
34. Lehoucq, R. B., Sorensen, D. C. & Yang, C. ARPACK Users' Guide (Society for Industrial and Applied Mathematics, 1998). https://epubs.siam.org/doi/pdf/10.1137/1.9780898719628.
35. Davanço, M., Urzhumov, Y. & Shvets, G. The complex Bloch bands of a 2D plasmonic crystal displaying isotropic negative refraction. *Opt. Exp.* **15**, 9681–9691. https://doi.org/10.1364/OE.15.009681 (2007).
36. Fietz, C., Urzhumov, Y. & Shvets, G. Complex k band diagrams of 3D metamaterial/photonic crystals. *Opt. Exp.* **19**, 19027–19041. https://doi.org/10.1364/OE.19.019027 (2011).
37. Raman, A. & Fan, S. Photonic band structure of dispersive metamaterials formulated as a Hermitian eigenvalue problem. *Phys. Rev. Lett.* **104**, 087401. https://doi.org/10.1103/PhysRevLett.104.087401 (2010).
38. Parisi, G., Zilio, P. & Romanato, F. Complex Bloch-modes calculation of plasmonic crystal slabs by means of finite elements method. *Opt. Exp.* **20**, 16690–16703. https://doi.org/10.1364/OE.20.016690 (2012).
39. Fang, C., Gilbert, M. J. & Bernevig, B. A. Bulk topological invariants in noninteracting point group symmetric insulators. *Phys. Rev. B* **86**, 115112. https://doi.org/10.1103/PhysRevB.86.115112 (2012).
40. Chong, Y. D., Wen, X.-G. & Soljačić, M. Effective theory of quadratic degeneracies. *Phys. Rev. B* **77**, 235125. https://doi.org/10.1103/PhysRevB.77.235125 (2008).

Acknowledgements

A.V.K. acknowledges fruitful discussions with M.G. Silveirinha. This work was partly supported by the Air Force Office of Scientific Research through Grant FA9550-21-1-0299. Work by T.C. is supported by Villum Fonden (42106).

Author contributions

Y.J. and B.Z. conceived the project. C.Q., Y.J., and A.V.K. performed numerical simulations assisted by J.J. and T.C. C.Q., Y.J., A.V.K., and B.Z. wrote the paper with input from all authors and C.Q. prepared figures 1–4. All authors discussed the results. B.Z. supervised the project.

Competing interests

The authors declare no competing interests.

Additional information

Supplementary Information The online version contains supplementary material available at https://doi.org/10.1038/s41598-023-47848-5.

Correspondence and requests for materials should be addressed to B.Z.